

Reconstructions of Jupiter's magnetic field using physics informed neural networks

Philip W. Livermore¹, Leyuan Wu², Longwei Chen³, Sjoerd de Ridder¹

¹School of Earth and Environment, University of Leeds, Leeds, LS2 9JT

²Key Laboratory of Quantum Precision Measurement of Zhejiang Province, Center for Optics and Optoelectronics Research (COOR), Center for Optics and Optoelectronics Research (COOR), Collaborative Innovation Center for Information Technology in Biological and Medical Physics, College of Science, Zhejiang University of Technology, Hangzhou, 310023, China.

³Guangxi Key Laboratory of Exploration For Hidden Metallic Ore Deposits, College of Earth Sciences, Guilin University of Technology, Guilin, 541006, China.

Key Points:

- We present two reconstructions of Jupiter's magnetic field using physics informed neural networks: PINN33, based on the first 33 orbits and PINN50, based on the first 50 orbits.
- Compared with spherical harmonic based methods, our reconstructions give a more stable downwards continuation and result in clearer images at depth of Jupiter's internal magnetic field
- Our models infer a dynamo at a fractional radius of 0.8.

Corresponding author: Phil Livermore, p.w.livermore@leeds.ac.uk

Abstract

Magnetic sounding using data collected from the Juno mission can be used to provide constraints on Jupiter’s interior. However, inwards continuation of reconstructions assuming zero electrical conductivity and a representation in spherical harmonics are limited by the enhancement of noise at small scales. In this paper we describe new reconstructions of Jupiter’s internal magnetic field based on physics-informed neural networks and either the first 33 (PINN33) or the first 50 (PINN50) of Juno’s orbits. The method can resolve local structures, and allows for weak ambient electrical currents. Compared with other methods, our reconstructions of Jupiter’s magnetic field both on and above the surface are similar, and we achieve a similar fit to the Juno data. However, our models are not hampered by noise at depth, and so offer a much clearer picture of the interior structure. We estimate that the dynamo boundary is at a fractional radius of 0.8. At this depth, the magnetic field is arranged into longitudinal bands, and the great blue spot appears to be rooted in neighbouring structures of oppositely signed flux.

Plain Language Summary

A major goal of the Juno mission is to better constrain the interior structure of Jupiter. One method of doing this is to reconstruct Jupiter’s magnetic field using measurements from Juno, which can then be used to probe the interior. One particular internal region of interest is the dynamo, within which the planetary magnetic field is generated. Standard assumptions of zero electrical conductivity and global solutions allow the reconstructions to be inwards extrapolated, however this method of imaging is limited by amplified noise. Here, we present reconstructions based on recent advances in machine learning, in which the physical assumptions are relaxed and we allow for local structures. Our method shows a much clearer image of Jupiter’s interior than has been possible before.

1 Introduction

The Juno mission, launched in 2011 (Bolton et al., 2010), has revolutionised our understanding of Jupiter’s interior through the collection of both gravity and magnetic measurements in orbit since 2016. These new data have not only allowed new constraints on the density structure and zonal flow in the outermost parts of the planet (Kaspi et al., 2018), but have permitted new reconstructions of the magnetic field to unprecedented resolution (e.g. Connerney et al., 2017, 2022). These magnetic maps highlight local features such as the Great Blue Spot, sited within a largescale hemispheric field (Moore et al., 2018) which shows evidence of secular variation (Ridley & Holme, 2016; Moore et al., 2019; Sharan et al., 2022; Bloxham et al., 2022; Connerney et al., 2022).

In order to infer the structure of Jupiter’s internally generated magnetic field, global reconstructions are needed that fit a physical model of the magnetic field to the sparse magnetic dataset collected on orbital trajectories. The physical model commonly adopted is that the measured values come from a region free from electrical currents, and comprise signals dominated by the internally generated field with more minor contributions from an external magnetic field and unmodelled instrumentation noise. Typical studies then proceed by subtracting an approximation to the external field assuming a magnetodisk structure, with estimates of the parameters (Connerney et al., 1981, 2022), although the difficulty in adopting an accurate representation is compounded by its unknown likely time-dependence (Ridley & Holme, 2016; Moore et al., 2019). The remaining signal is then fit in a least-squares sense to an analytic description of an internally-generated magnetic field \mathbf{B} using a potential V , with $\mathbf{B} = -\nabla V$, which by construction exactly satisfies $\mathbf{J} = \mathbf{0}$ where \mathbf{J} is the ambient electrical current. The potential is then typically represented in terms of a truncated spherical harmonic expansion (Connerney, 1981), similar to comparable studies for Earth’s magnetic field (e.g. Alken et al., 2021).

Such reconstructions allow not only spatial interpolation between the Juno measurements, but also extrapolation into regions unconstrained by measurements. Downwards continuation radially inwards under Jupiter’s surface, assuming the same electrically-insulating physics, is of particular interest because it allows inference of the dynamo radius, typical values for which are $0.8 - 0.83R_J$, where R_J is Jupiter’s equatorial radius (71,492km) (Connerney et al., 2022; Sharan et al., 2022). However, this downwards continuation is numerically unstable because errors in small-scales, caused by leakage from unmodelled signals, become amplified more rapidly with decreasing radius than errors in large-scales, eventually producing a signal swamped with noise.

In this paper, we propose a novel representation of Jupiter’s internal magnetic field based on physics informed neural networks (PINNs). Compared to standard approaches, our models give a similar reconstruction on and above Jupiter’s surface but appear to be more stable under downwards continuation. In the following sections, we first describe the data before outlining our PINN approach. We present some reconstructions and estimates of the dynamo radius, which we compare with those from existing methods, and end with a brief discussion.

2 Data

Our work is based the vector magnetic field measured by Juno within the first 50 perijoves during the period 2016 to 2023, which contains the prime mission of 33 orbits. From these data we excluded the second perijove (PJ2) due to a spacecraft safe mode entry Connerney et al. (2018). The original observations were down-sampled to 30 s sampling rate (this being the approximate rotation time of the spacecraft) using a mean-value filter. In order to maximise the internal signal content of the data, we used only measurements recorded at planetocentric spherical radius $r \leq 4.0R_J$ (where $R_J = 71,492$ km, the equatorial radius). In total, there were 28011 3-component measurements of the magnetic field, of periapsis $1.02 R_J$ and taking magnitudes in the range of approximately 0.065 – 16 Gauss. Figure 1 shows an overview of the data used in this work.

3 Method

Physics informed neural networks, or PINNs, offer a technique for representing spatially dependent quantities by a neural network that are constrained not only by data but also physical laws (Raissi et al., 2019). There are two key differences between a PINN representation and existing reconstructions based on a spherical-harmonic potential. First, existing methods fit data in a weak sense (by least squares) to physics imposed in a strong form (by assuming an internal potential field representation). This is quite different in a PINN, where both data and physics are fit in a weak form, which makes them particularly effective in problems when the data and physics are imperfectly known (Karniadakis et al., 2021), as for Jupiter. Instead of assuming that $\mathbf{J} = 0$ and seeking a fit to an internally-generated magnetic solution, instead we minimising the root-mean-squared electrical current \mathbf{J} which allows, for example, weak nonzero electric currents if the data require them. Another key distinction is that we don’t (and indeed cannot) separate internal and external fields as we fit the PINN to the fundamental physical law, rather than to an analytic solution which assumes the location of source.

A second important difference is in the spatial representation. A spherical harmonic representation, an analytic solution to Laplace’s equation, is defined by a set of Gauss coefficients, whose globally resolved wavelength is approximately $2\pi/(N+1/2)$, where N is the maximum degree N (Backus et al., 1996). In contrast, a neural network is a meshless method that can define both local and global solutions. It is defined by a set of weights and biases that describe the internal coefficients of connected neurons, arranged in a structure that is governed by various hyperparameters: the number of neurons per layer, the number of layers, and the activation function.

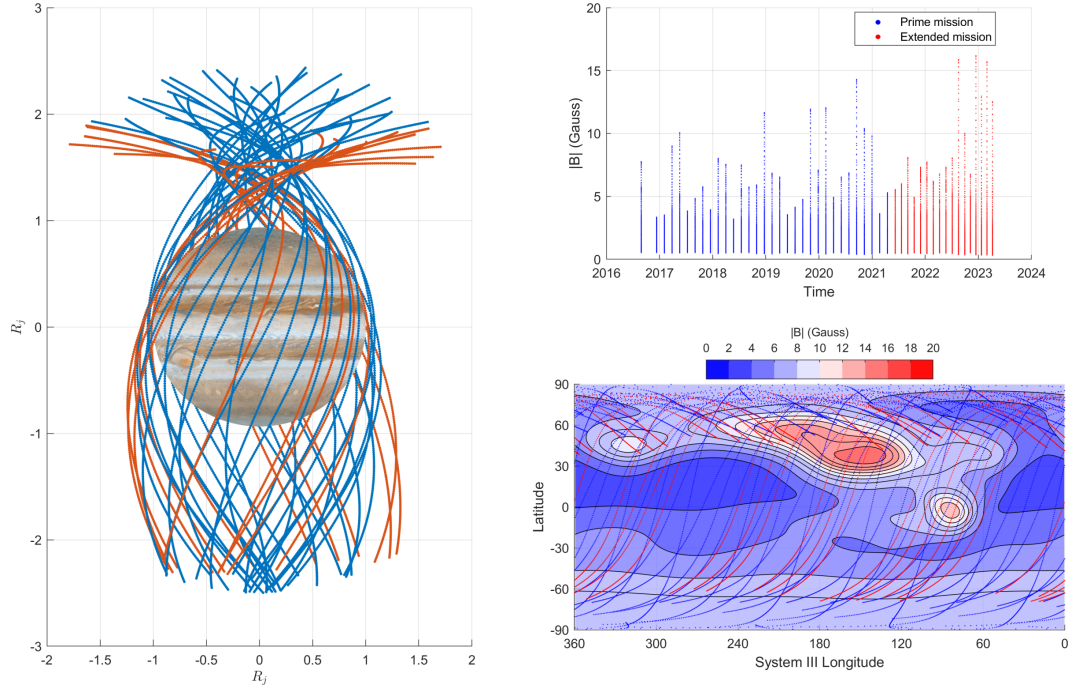


Figure 1. Juno data used in this work. Left: Juno’s global coverage after 50 orbits, showing Juno’s trajectory within radius $2.5 R_J$; the colours show the 33 prime mission orbits (red lines) and extended mission (blue lines). Upper right: time span and magnitude range per orbit of Juno magnetic data. Lower right: orbital position (radius within $4.0 R_J$) projected onto a background contour map of the magnitude of magnetic field at $r = R_J$ reconstructed using model PINN50e.

We work in a planetocentric Cartesian coordinate system, and write the magnetic field in terms of a vector-potential: $\mathbf{B} = \nabla \times \mathbf{A}$, which satisfies the fundamental relation $\nabla \cdot \mathbf{B} = 0$. The three independent components of \mathbf{A} , (A_x, A_y, A_z) , are expressed as individual feed-forward neural networks (FNNs) with 6 hidden layers, 40 neurons per layer and swish activation functions. We rescale the input $\mathbf{r} = (x, y, z)$ coordinates to $[-1, 1]^3$, but leave the data unscaled as it is handled by an appropriate dynamic weighting.

We denote the set of tunable parameters (weights and biases) of the networks by Θ , and the representation of \mathbf{A} and \mathbf{B} as $\mathbf{A}_\Theta(\mathbf{r})$ and $\mathbf{B}_\Theta(\mathbf{r})$. A physics-informed model is trained by minimizing the following loss function:

$$\mathcal{L}(\Theta) = w_d \mathcal{L}_d(\Theta) + w_p \mathcal{L}_p(\Theta), \quad (1)$$

where

$$\mathcal{L}_d(\Theta) = \frac{1}{N_d} \sum_i^{N_d} |\mathbf{B}_\Theta(\mathbf{r}_d^i) - \mathbf{B}(\mathbf{r}_d^i)|^2, \quad \mathcal{L}_p(\Theta) = \frac{1}{N_p} \sum_i^{N_p} |(\nabla \times \mathbf{B}_\Theta)(\mathbf{r}_p^i)|^2, \quad (2)$$

are the data misfit and physics loss terms with weights w_d and w_p , N_p , \mathbf{r}_p^i are the number and location of the collocation points used to constrain the physics loss, and N_d are the number of Juno data used, each of which has location \mathbf{r}_d^i and vector value $\mathbf{B}(\mathbf{r}_d^i)$. The contribution to the data loss from each measurement is assumed equal, as is the contribution to the physics loss from each of the collocation points. The quantities derived from \mathbf{A}_Θ , namely $\mathbf{B}_\Theta(\mathbf{r})$ and $\nabla \times \mathbf{B}_\Theta = \nabla(\nabla \cdot \mathbf{A}_\Theta) - \nabla^2 \mathbf{A}_\Theta$ are computed using automatic differentiation (AD) (Baydin et al., 2018). All neural network models are built with the machine learning framework TensorFlow (Abadi et al., 2016), and trained with the built-in Adam optimizer (Kingma & Ba, 2015) over 12,000 epochs with batch size 10,000. An empirical learning-rate annealing strategy, with an initial learning rate of 0.002, and an exponential decay with a decay rate of 0.8 and a decay step of 1,000 iterations are adopted. From a limited number of tests of various network sizes, this network was just large enough to fit well all the data and physics constraints. We do not use any explicit spatial regularisation in our method.

Despite success across a range of applications, the original formulation of Raissi et al. (2019) sometimes struggles to converge on an accurate solution; here we apply two techniques to improve the method. First, rather than prescribe the weight parameters w_d and w_p , we allow them to be chosen dynamically. We fix $w_p = 1$, but allow w_d to change at each training epoch in order to balance the gradients of physical and data-fit loss with respect to the model parameters (Wang et al., 2021). Second, we adopt residual-based sampling for the physics loss term. While uniformly sampled collocation points for the physics term offers a simple approach, recent studies have shown promising improvements in training accuracy by applying nonuniform adaptive sampling strategies (Lu et al., 2021; Nabian et al., 2021; Wu et al., 2023). Here we apply a simplified version of the residual-based adaptive distribution (RAD) method described in Wu et al. (2023). For the first 3000 epochs we use a uniformly sampled set of points in a fixed region, but at epoch 3000 (and every 600 epochs thereafter) we create a pdf, based on samples of the physics loss, which we use to resample the collaboration points, effectively increasing the local weighting in regions with a high physics loss.

We create four PINN models, based on either the first 33 (PINN33i, PINN33e) or 50 Juno orbits (PINN50i, PINN50e), assuming for each that the magnetic field is static. We deliberately distinguish between models internal to Jupiter (denoted by the character:i) which downwards continue into $r \leq R_J$ the data observed in $r > R_J$, and those external to Jupiter (denoted by the character:e) which interpolate data within the same region in which Juno measurements are made $r > R_J$. Models PINN50e, PINN33e were made first, using 300,000 collocation points within the region $1 \leq r/R_J \leq 4$. Models

PINN50i and PINN33i were then constructed, using 40,000 collocation points within the region $0.8 \leq r/R_J \leq 1$; the data loss term was replaced by a term describing matching in each component to either PINN50e or PINN33e on $r = R_J$ at 80,000 randomly located points. Although mildly oblate, Jupiter is assumed spherical for simplicity.

4 Results and discussion

Figure 2 shows an orbital comparison of Juno data with four models: PINN33e, PINN50e and two recent spherical harmonic models JRM33 ($N = 18$) (Connerney et al., 2022) and the Baseline model of Bloxham et al. (2022) with $N = 32$. These recent models have been chosen because although they are both based on the first 33 orbits, they differ in how the spherical harmonics are fitted: JRM33 uses an approach based on singular value decomposition, whereas the Baseline model uses regularisation. A simple external dipole approximation to the external field (Connerney et al., 2022) has been added to the spherical harmonic models, as they only represent the internal field; the PINN models represent both internal and external field.

The models based only on the prime orbits (1-33, excluding 2): PINN33e, JRM33 and Baseline show a comparable absolute rms error. For the majority of orbits, PINN33e has an error less than JRM33, with a few exceptions such as orbit 32. Over the first 33 orbits, the rms error for JRM33 is 774.1 nT, compared with 509.3 nT for Baseline and 511.4 nT for PINN33e. Using these models for orbits 34-50 leads to increasing discrepancy with the measurements, providing additional evidence for Jupiter's secular variation. Model PINN50e has a slightly higher rms of 589.7 nT for orbits 1-33, but fits the data for orbits 34-50 much better because it has been trained in part on these data.

The structure of JRM33, Baseline and PINN50i at radii $r/R_J = 1, 0.95, 0.9, 0.85, 0.8$ are shown by contours of radial field in figure 3. On $r = R_J$ the models are almost indistinguishable in terms of physical structure, but as the radius decreases and we (presumably) get closer to the dynamo source, the signal strength increases and the length-scales decrease. The instability of downwards continuation in the spherical harmonic models is readily apparent by the prevalent fine-scaled noise, particularly in the azimuthal direction. By comparison, PINN50i remains relatively free of noise and the features at depth are much easier to identify.

At $r \leq 0.85R_J$, the field appears arranged into longitudinal bands, with a strong band at high latitude and a weaker band near the equator. Many of the strong patches of flux have adjacent oppositely signed counterparts, as can be seen in particular around the root of the great blue spot. The hemispheric structure is also striking, with almost all the magnetic structure of the field being confined north of the equator.

A common approach to determining the dynamo radius is by determining where the Lowes-Mauersberger spectrum of the magnetic field (Lowes, 1974; Mauersberger, 1956) is flat, which describes a white-noise source. This procedure relies on the spherical harmonic representation of the magnetic field:

$$\mathbf{B} = -R_J \nabla \sum_{n=0}^N \sum_{m=0}^n \left(\frac{R_J}{r} \right)^{n+1} [g_n^m P_n^m(\theta) \cos(m\phi) + h_n^m P_n^m(\cos \theta) \sin(m\phi)] \quad (3)$$

where g_n^m and h_n^m are the Gauss coefficients of degree n and order m and P_n^m are associated Legendre functions. The spectrum is then derived as

$$R_n = (n+1) \left(\frac{R_J}{r} \right)^{(2n+4)} \sum_{m=0}^n (g_n^m)^2 + (h_n^m)^2 \quad (4)$$

In order to find the spectrum for the PINN models, we have two options. First is analytic continuation, where we project the field at $r = R_J$ onto (3) and use the inherent

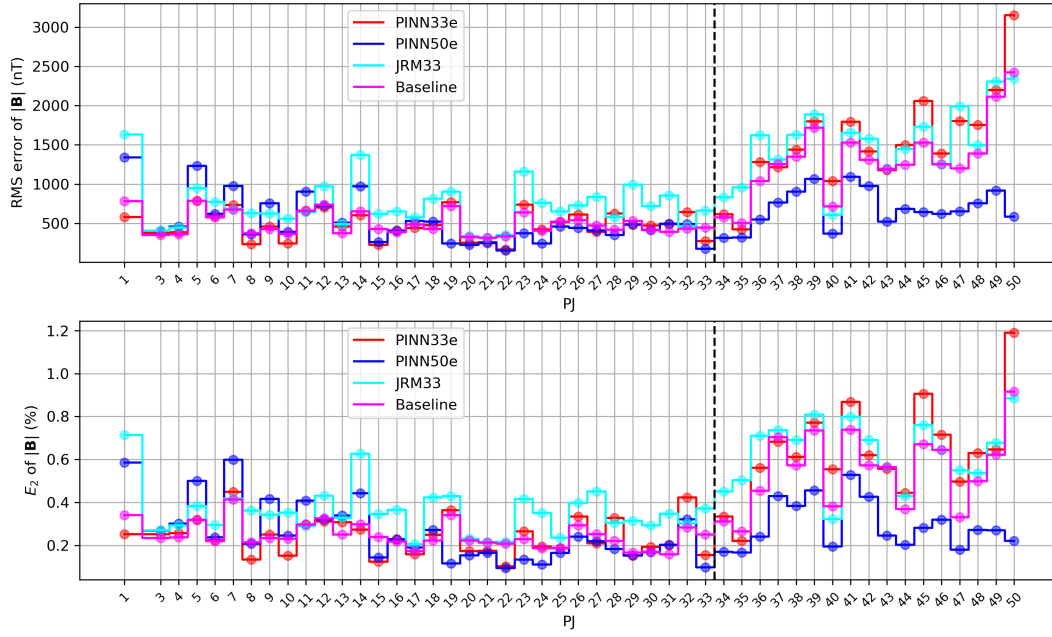


Figure 2. Orbital comparison of the discrepancy between various reconstructions of Jupiter’s magnetic field: PINN33e, PINN50e, JRM33 and Baseline, with the Juno data. Taking each orbit in turn, the error is quantified by taking the root mean squared value of the difference in magnitude of the reconstructed magnetic field with the magnitude of each vector measurement. We show the (upper) absolute value of this error, and (lower) relative value of this error compared to the rms observed magnitude over the orbit. The dashed line delineates the prime from the extended mission.

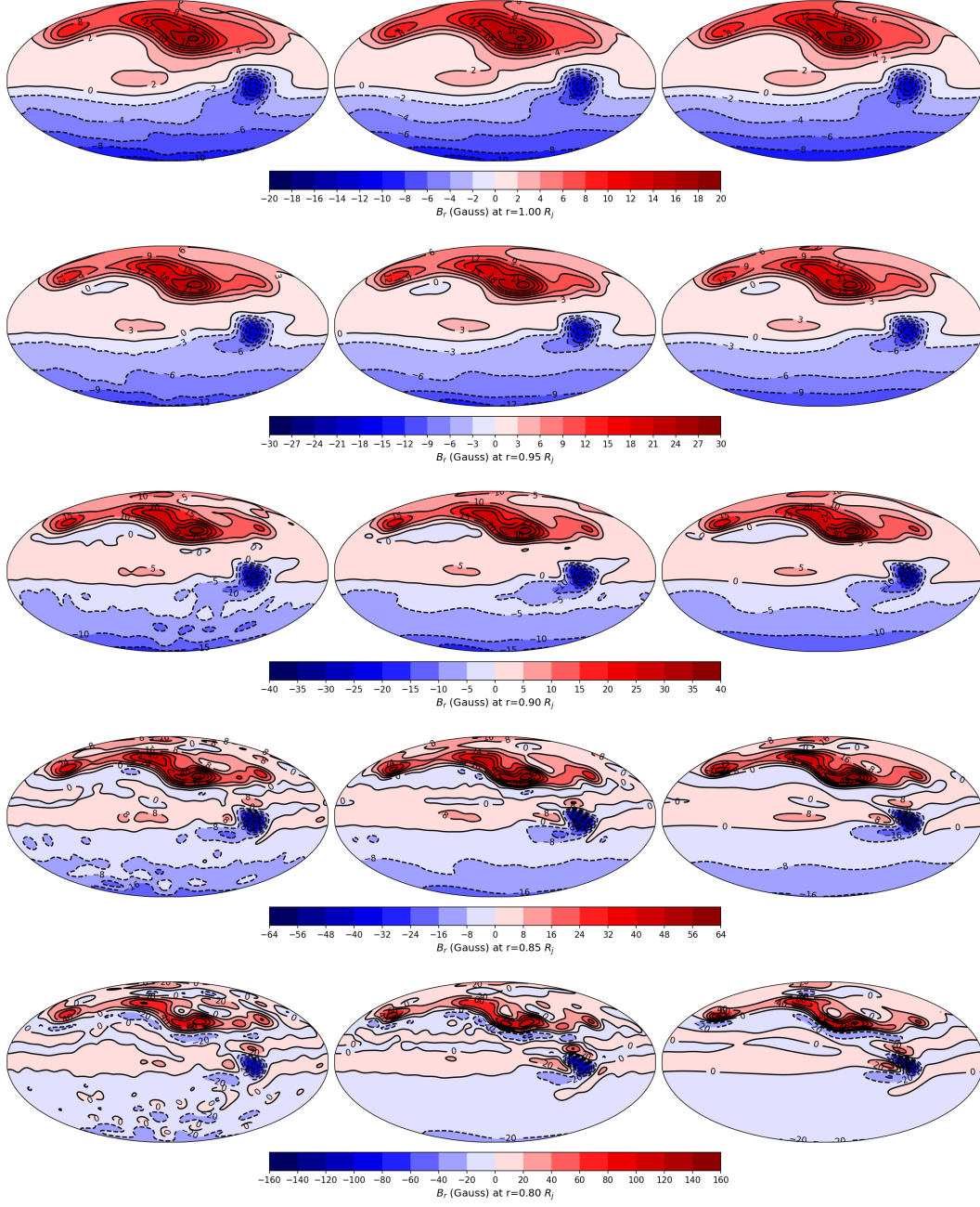


Figure 3. The radial component of Jupiter's magnetic field on various spherical radii inside Jupiter's surface. The plots are shown on a Mollweide projection with the central meridian at a longitude of 180° west (System III coordinates). Left column shows the JRM33 model ($N = 18$) (Connerney et al., 2022), the middle column shows the Baseline model (Bloxham et al., 2022) ($N = 32$) and the right column shows the PINN model PINN50i.

radial dependence within (4). This procedure removes any external field within the PINN model. Second, we can use PINN extrapolation, for which we use PINN50i to downwards continue, and at each radius $\tilde{r} < R_J$, project onto (3) and then use (4) at $r = \tilde{r}$. Any externally produced field will still be present in the model, albeit at assumed large length-scales. In either case, we find the Gauss coefficients by performing a spherical harmonic transform of the spherically radial component B_r .

Figure 4 shows the Lowes-Mauersberger spectrum as a function of degree n for JRM33, Baseline and PINN50i (solid lines: analytic continuation, black symbols, PINN extrapolation). At $r = R_J$ the spectral power for degrees 2–18 agrees well between the models and falls off exponentially with n . The power in the dipole is higher than this simple profile predicts. As the radius is decreased the profile flattens as the smaller scales become more prominent. Above degree 18, the three analytically continued models diverge, with JRM33 having the most power at high degree. Of the three models, the Baseline model (which is the only model with explicit regularisation) has the least power at small-degree. For degrees higher than about 18 it is striking that the analytic and PINN extrapolation methods diverge, with the PINN extrapolation having smaller power at high-degree. These two methods, by construction, agree on $r = R_J$, and as the radius decreases the discrepancy gets larger.

We quantify the slope of the spectrum by fitting a straight line to $\log_{10} R_n(n)$ for degrees 2–18. The lower panel of figure 4 shows the slope variation with radius for four models analytically inwards continued using (3). On making the assumption that the slope is zero at the source we infer that the dynamo radius is about $r = 0.8R_J$, in approximate agreement with other studies (Connerney et al., 2022; Sharan et al., 2022).

5 Concluding remarks

We have presented a reconstruction of Jupiter’s magnetic field, based on data from Juno within the framework of a physics informed neural network. Our reconstructions have a similar misfit to the data compared with other spherical harmonic methods, and produce a similar structure of magnetic field on Jupiter’s surface. However, by using a meshless method, and only weakly constraining the (poorly known) physics, our models are not apparently hostage to the typically enhanced noise with decreasing radius. Compared with spherical harmonic-based methods, we produce a clearer picture at depth of the localised interior magnetic field.

The fact that most of the structure in Jupiter’s field appears confined to the northern hemisphere perhaps makes neural networks a particularly effective modelling tool. Even at modest resolution, neural networks are able to very well represent local structures, compared to spherical harmonics which are inherently global. More broadly, the reduction of noise in the reconstructed field at depth may better constrain secular changes close to the dynamo region, which is the subject of a forthcoming study.

Data Availability Statement

The original Juno magnetometer data are publicly available on NASA’s Planetary Data System (PDS) at Planetary Plasma Interactions (PPI) node at <https://pds-ppi.igpp.ucla.edu/search/?sc=Juno&t=Jupiter&i=FGM>. The produced PINN models, together with input processed Juno data, spherical harmonic models, and all related Python code and Jupyter notebook to reproduce all the results in this work, are archived in the Github repository https://github.com/LeyuanWu/JunoMag_PINN.VP3.

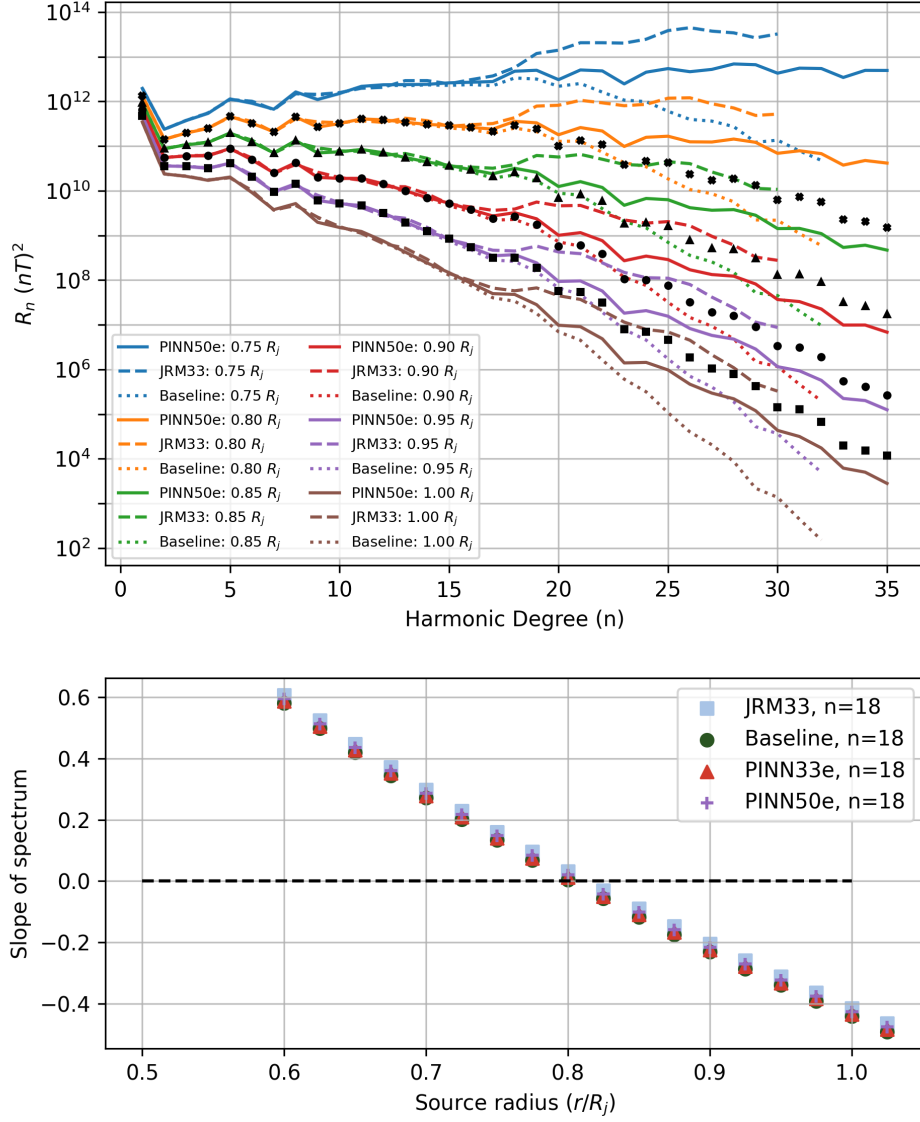


Figure 4. Upper panel: Coloured lines show the Lowes-Mauersberger spectrum of three analytically continued models: PINN50e, (to degree $n = 35$), JRM33 (using the full $n = 30$ resolution) and Baseline ($n = 32$). Black symbols show spectra obtained from PINN extrapolation using PINN50i in $r < R_J$ (cross: $0.80R_J$; triangle: $0.85R_J$; circle: $0.90R_J$; square: $0.95R_J$). Lower panel: spectral slope with radius assuming analytic continuation, fit to degrees 2–18 for models JRM33, Baseline, PINN33e and PINN50e.

Acknowledgments

This study was funded by the National Natural Science Foundation of China (Grant No. 42374173), National Natural Science Foundation of Guangxi Province of China (Grant No. 2020GXNSFDA238021). This work was undertaken on ARC4, part of the High Performance Computing facilities at the University of Leeds, UK. We thank Jack Connerney for help with accessing the Juno data.

References

- Abadi, M., Barham, P., Chen, J., Chen, Z., Davis, A., Dean, J., . . . Zheng, X. (2016). Tensorflow: a system for large-scale machine learning. In *Proceedings of the 12th usenix conference on operating systems design and implementation* (p. 265–283). Savannah, GA, USA: USENIX Association.
- Alken, P., Thébaud, E., Beggan, C. D., Amit, H., Aubert, J., Baerenzung, J., . . . others (2021). International geomagnetic reference field: the thirteenth generation. *Earth, Planets and Space*, 73(1), 1–25.
- Backus, G., Parker, R. L., & Constable, C. (1996). *Foundations of geomagnetism*. Cambridge University Press.
- Baydin, A. G., Pearlmutter, B. A., Radul, A. A., & Siskind, J. M. (2018). Automatic differentiation in machine learning: a survey. *Journal of Machine Learning Research*, 18, 153.
- Bloxham, J., Moore, K. M., Kulowski, L., Cao, H., Yadav, R. K., Stevenson, D. J., . . . Bolton, S. J. (2022). Differential rotation in jupiter’s interior revealed by simultaneous inversion for the magnetic field and zonal flux velocity. *Journal of Geophysical Research: Planets*, 127(5), e2021JE007138.
- Bolton, S., Team, J. S., et al. (2010). The juno mission. *Proceedings of the International Astronomical Union*, 6(S269), 92–100.
- Connerney, J. E. P. (1981). The magnetic field of jupiter: A generalized inverse approach. *Journal of Geophysical Research: Space Physics*, 86(A9), 7679–7693.
- Connerney, J. E. P., Acuna, M. H., & Ness, N. F. (1981). Modeling the jovian current sheet and inner magnetosphere. *Journal of Geophysical Research: Space Physics*, 86(A10), 8370–8384.
- Connerney, J. E. P., Benn, M., Bjarno, J. B., Denver, T., Espley, J., Jorgensen, J. L., . . . Smith, E. J. (2017). The juno magnetic field investigation. *Space Science Reviews*, 213(1-4), 39–138. doi: 10.1007/s11214-017-0334-z
- Connerney, J. E. P., Kotsiaros, S., Oliverson, R. J., Espley, J. R., Joergensen, J. L., Joergensen, P. S., . . . Levin, S. M. (2018). A new model of jupiter’s magnetic field from juno’s first nine orbits. *Geophysical Research Letters*, 45(6), 2590–2596. doi: 10.1002/2018GL077312
- Connerney, J. E. P., Timmins, S., Oliverson, R. J., Espley, J. R., Joergensen, J. L., Kotsiaros, S., . . . Levin, S. M. (2022). A new model of jupiter’s magnetic field at the completion of juno’s prime mission. *Journal of Geophysical Research-planets*, 127(2), e2021JE007055. doi: 10.1029/2021JE007055
- Karniadakis, G. E., Kevrekidis, I. G., Lu, L., Perdikaris, P., Wang, S., & Yang, L. (2021). Physics-informed machine learning. *Nature Reviews Physics*, 3(6), 422–440.
- Kaspi, Y., Galanti, E., Hubbard, W. B., Stevenson, D., Bolton, S., Iess, L., . . . others (2018). Jupiter’s atmospheric jet streams extend thousands of kilometres deep. *Nature*, 555(7695), 223–226.
- Kingma, D. P., & Ba, J. (2015). *Adam: A method for stochastic optimization*. Retrieved from <http://arxiv.org/abs/1412.6980>
- Lowes, F. (1974). Spatial power spectrum of the main geomagnetic field, and extrapolation to the core. *Geophysical Journal International*, 36(3), 717–730.
- Lu, L., Meng, X. H., Mao, Z. P., & Karniadakis, G. E. (2021). Deepxde: A deep learning library for solving differential equations. *Siam Review*, 63(1), 208–228. doi: 10.1137/19M1274067
- Mauersberger, P. (1956). Das mittel der energiedichte des geomagnetischen hauptfeldes an der erdoberfläche und seine saulare andernung. *Gerlands Beitr. Geophys.*, 65, 207–215.
- Moore, K. M., Cao, H., Bloxham, J., Stevenson, D., Connerney, J., & Bolton, S. (2019). Time variation of jupiter’s internal magnetic field consistent with zonal

- 317 wind advection. *Nature Astronomy*, 3(8), 730–735.
- 318 Moore, K. M., Yadav, R. K., Kulowski, L., Cao, H., Bloxham, J., Connerney, J. E.,
 319 ... others (2018). A complex dynamo inferred from the hemispheric dichotomy of
 320 jupiter’s magnetic field. *Nature*, 561(7721), 76–78.
- 321 Nabian, M. A., Gladstone, R. J., & Meidani, H. (2021). Efficient training
 322 of physics-informed neural networks via importance sampling. *Computer-
 323 Aided Civil and Infrastructure Engineering*, 36(8), 962–977. Retrieved from
 324 <https://onlinelibrary.wiley.com/doi/abs/10.1111/mice.12685> doi:
 325 <https://doi.org/10.1111/mice.12685>
- 326 Raissi, M., Perdikaris, P., & Karniadakis, G. E. (2019). Physics-informed neural
 327 networks: A deep learning framework for solving forward and inverse problems in-
 328 volving nonlinear partial differential equations. *Journal of Computational Physics*,
 329 378, 686–707. doi: 10.1016/j.jcp.2018.10.045
- 330 Ridley, V. A., & Holme, R. (2016). Modeling the jovian magnetic field and its sec-
 331 ular variation using all available magnetic field observations. *J.Geophys. Res.:
 332 Planets*, 121(3), 309–337.
- 333 Sharan, S., Langlais, B., Amit, H., Thebault, E., Pinceloup, M., & Verhoeven,
 334 O. (2022). The internal structure and dynamics of jupiter unveiled by a high-
 335 resolution magnetic field and secular variation model. *Geophys. Res. Lett.*, 49(15),
 336 e2022GL098839.
- 337 Wang, S. F., Teng, Y. J., & Perdikaris, P. (2021). Understanding and mitigating
 338 gradient flow pathologies in physics-informed neural networks. *Siam Journal on
 339 Scientific Computing*, 43(5), A3055–A3081. doi: 10.1137/20M1318043
- 340 Wu, C. X., Zhu, M., Tan, Q. Y., Kartha, Y., & Lu, L. (2023). A comprehensive
 341 study of non-adaptive and residual-based adaptive sampling for physics-informed
 342 neural networks. *Computer Methods in Applied Mechanics and Engineering*, 403,
 343 115671. doi: 10.1016/j.cma.2022.115671